Plasma Assisted NH_3/H_2/Air Ignition in Nanosecond Discharges with Non-Equilibrium Energy Transfer

Zhiyu Shi[a], Xingqian Mao[a,*], Ziyu Wang[a,c], Yiguang Ju[a,b]

[a] *Department of Mechanical and Aerospace Engineering, Princeton University, Princeton, NJ 08544, USA*

[b] *Princeton Plasma Physics Laboratory, Princeton, New Jersey 08540, USA*

[c] *Department of Mechanical and Aerospace Engineering, Utah State University, Logan, UT 84322, USA*

*Corresponding author: xingqian@princeton.edu

Abstract: Ammonia (NH_3), with its high energy density and easiness to store and transport as a hydrogen carrier, has become a promising alternative green fuel. However, its adoption in power generation is hindered by challenges such as low burning velocity, slow low-temperature oxidation, NO_x emissions, and ignition difficulty. This work computationally investigates the effects of non-equilibrium energy transfer by nanosecond discharges on NH_3 ignition and flame propagation in an NH_3/H_2/air flow at 700 K and 1 atm. The simulation results demonstrate that NH_3/air mixtures require a large ignition energy due to their large critical ignition radius. It is shown that adding 30% hydrogen significantly reduces the critical ignition radius and minimum ignition energy. Two-dimensional modeling further shows a non-monotonic dependence of ignition kernel volume on the applied voltage and reduced electric field. The optimum ignition enhancement occurs at 200 Td where the generation of electronically excited species and radicals including $N_2(B)$, $O(^1D)$ and OH becomes most efficient. Higher voltages divert electron energy toward ionization, which makes it less effective for NH_3 ignition. The study also identifies an optimal electrode gap size for a given pulse energy. Smaller gap sizes increase deposited energy density, raising temperature and radical concentrations. However, excessive reduction of the gap distance reduces flame propagation speed due to the flame stretch effect in rich mixtures with the effective Lewis number greater than unity. A nonlinear relationship between pulse repetition frequency and ignition kernel volume is observed in a nanosecond pulsed high frequency discharge (NPHFD). An optimal frequency range of 200 kHz to 2 MHz is found when two pulses are used. In addition, an optimal number of pulses exists for each pulse repetition frequency, with higher frequencies requiring more pulses to maximize the overlap region. These findings provide critical insights on developing controlled plasma discharge techniques for efficient NH_3 ignition in reactive flows within internal combustion engines and gas turbines.

Keywords: Ammonia; Plasma assisted ignition; Non-equilibrium energy transfer; Efficient ignition; Nanosecond pulsed discharge.

Novelty and significance:

The efficient combustion of ammonia (NH_3) represents a key strategy for achieving a carbon-neutral future, though its practical application is hindered by inherently low laminar flame speed. Non-equilibrium plasma presents a viable solution to overcome this challenge. This research numerically investigates plasma-assisted ignition and flame propagation using nanosecond discharges. It is the first comprehensive analysis of how varying non-equilibrium conditions - such as applied voltages, electrode gap sizes, pulse repetition frequencies, and pulse numbers - impacts ignition in an NH_3/H_2/air flow using a multi-dimensional approach. The focus is to control non-equilibrium energy transfer for efficient NH_3 combustion in reactive flows by strategically manipulating electron energy deposition pathways, modifying energy distribution within the discharge region, and promoting the continuous accumulation of radicals. This work not only sheds light on the fundamental science behind NH_3 combustion but also enhances its viability as a sustainable fuel in internal combustion engines and gas turbines.

Author contributions:

Zhiyu Shi: Formal analysis, Methodology, Writing – original draft;

Xingqian Mao: Conceptualization, Methodology, Supervision, Writing – review & editing;

Ziyu Wang: Writing – review & editing;

Yiguang Ju: Conceptualization, Supervision, Writing – review & editing.

1. Introduction

In recent decades, the COP21 Paris Agreement [1] has driven significant efforts toward decarbonizing energy generation. Among various alternative fuels, ammonia (NH_3) stands out as a promising candidate [2-6]. Produced from renewable resources and containing 17.8% hydrogen by mass, it offers several key advantages: high hydrogen content and easier for liquefaction, storage, and transportation. These features make it a promising alternative to hydrogen (H_2) [2-3]. Despite its century-long history in industrial use, the application of ammonia as a fuel still faces many challenges. The low burning velocity, high NO_x emissions, slow low-temperature oxidation and ammonia slip all hinder the application of ammonia in engines and gas turbines [7-8]. Therefore, enhancing ignition and low-temperature oxidation of ammonia is crucial for its successful implementation in power generation.

One effective strategy to address these limitations is blending NH_3 with fuel with higher reactivity [9-12]. Compared with hydrocarbons, an appropriate proportion of H_2 can enhance NH_3 combustion while mitigating safety concerns associated with H_2 [13] as well as avoiding carbon emissions and toxic byproducts. In NH_3/H_2/air flames, the addition of H_2 promotes a larger pool of O/H radicals through fast chain-branching reactions, leading to a higher burning velocity and lower ignition energy. For example, research by Zhang et al. [10] demonstrated that the primary chain-branching reaction shifts from $NH_2 + NO = NNH + OH$ to $H + O_2 = O + OH$ with an increased H_2 content, which promotes the consumption of NH_3. Mai et al. [14] experimentally investigated the influence of the Lewis number, pressure, and spark gap on the flow-facilitated ignition (FFI) phenomenon in electrode-spark (forced) ignition for NH_3/H_2/air mixtures.

Additionally, advancements in plasma-assisted ignition technologies have introduced new possibilities for overcoming the challenges of NH_3 ignition [15-16]. Nanosecond discharges (NSD), in particular, play a crucial role by effectively generating electrons, excited species, radicals, and ions, significantly lowering the energy barrier for ignition [17-19]. These discharges initiate new non-equilibrium pathways at low temperatures, enabling enhanced NH_3 combustion. Various studies, both experimentally and numerically, have explored the impact of non-equilibrium plasma on NH_3 combustion [20-27]. Choe et al. [20] reported that plasma can simultaneously reduce NO_x emission and extend the lean blowoff limits in premixed swirling flames. Shy et al. [21] demonstrated experimentally that NSD at a pulse repetition frequency improves ignition and reduces minimum ignition energy for both fuel-lean and fuel-rich conditions compared to conventional sparks. To understand the kinetic enhancement by plasma, Zhong et al. [15] explored plasma-assisted NH_3 oxidation at room temperature for the first time and developed a $NH_3/O_2/N_2$ plasma-combustion kinetic model based on *in-situ* laser diagnostics and plasma modeling. Central to the effectiveness of plasma-assisted ignition is the control of non-equilibrium energy transfer. Mao et al. [22] computationally studied plasma-assisted low temperature NH_3/air ignition in a repetitively-pulsed nanosecond discharge using this model. They found that the optimum ignition enhancement is achieved at the

reduced electric field where the production of electronically excited species and radicals is most efficient. Similar phenomena have also been experimentally observed in plasma-assisted methane–air oxidation [23] and H_2-O_2 low-pressure combustion [24]. Liu et al. [25] combined time-resolved *in-situ* laser diagnostics with plasma modeling to investigate plasma-assisted NH_3/H_2 oxidation. The results showed that at a high reduced electric field, when the H_2 blending ratio increases, the NH_3 oxidation is promoted differently due to both HO_2 formation and strong NO kinetic enhancement via NO-HO_2 and NO_2-H pathways. These studies dramatically advance the understanding of the enhancement of non-equilibrium plasma on NH_3 combustion.

Despite these insights, existing research often relies on simplistic models that do not fully capture the complex dynamics of plasma discharge and flame propagation necessary for practical applications in internal combustion engines and gas turbines. Efficient NH_3 ignition and sustained combustion in these systems are vital for high performance and meeting stringent environmental standards. Multi-dimensional electrode geometry needs to be used to optimize ignition enhancement, with the ignition probability determined by the interplay among heat release, radical production, convective heat loss, and radical quenching due to fluid motion. Mao et al. [28] developed the two-dimensional (2-D) multi-scale adaptive reduced chemistry solver for plasma-assisted combustion (MARCS-PAC) and investigated the streamer propagation, its transition to spark and the ignition kernel development in a quiescent H_2/air mixture. The simulations revealed that the ignition enhancement was sensitive to the variation of electrode shape, diameter, and gap size due to the changes of electric field distribution and locations of streamer formation. The experiments of CH_4/air ignition using nanosecond pulsed discharge in a convective flow by Lefkowitz and Ombrello [29-30] also showed that the discharge interelectrode distance played an important role in the generation of effective ignition kernels. Recently, the application of nanosecond pulsed high frequency discharge (NPHFD) in reactive flows [29, 31, 32] has drawn great attention. Castela et al. [33] and other works [34-36] incorporated a phenomenological nanosecond repetitively pulsed discharge model into a 3-D fluid solver and applied it to investigate a sequence of discharge pulses in air and methane–air mixtures under both quiescent and turbulent flow configurations. Although the interactions between the ignition kernel development and the properties of the turbulent flow are captured, this model relies on physical approximations and empirical parameters which limits its ability to capture energy transfer processes and dynamics in non-equilibrium plasma. Compared with MARCS-PAC, this model fails to predict the streamer propagation, its transition to spark, the ignition kernel development, the non-uniform distributions of electric field, temperature and species concentrations with different electrode geometries, as well as the synergetic effects between plasma discharge and ignition kernel development. Mao et al. [37] applied the MARCS-PAC model to NPHFD and found that for a given total discharge energy with multiple pulsed discharges, the enhancement of the ignition kernel volume had a non-monotonic dependence on discharge frequency and pulse number in a plasma-

assisted H_2/air flow. Unfortunately, few studies have been conducted to examine the effect of non-equilibrium excitation in plasma as well as electrode geometry and voltage form on ammonia ignition. Since NH_3 has different combustion characteristics such as flame speed and the critical ignition radius, it is necessary to study the effects of non-equilibrium excitation by plasma on NH_3 ignition and flame propagation in a multi-dimensional discharge.

The goal of this study is to understand how to control non-equilibrium energy transfer for efficient NH_3 ignition and flame propagation in reactive flows. First, 2-D simulations of plasma-assisted ignition and flame propagation in an NH_3/H_2/air flow using nanosecond discharges are conducted. The effects of H_2 blending on NH_3 ignition are analyzed by calculating the critical radius and the ignition kernel growth. Secondly, the effects of applied voltage on electron energy deposition pathways and ignition enhancement are investigated. Then, the effects of electrode gap size on ignition kernel formation and flame propagation are studied. Finally, the effects of pulse repetition frequency and pulse number with a fixed total discharge energy on radical accumulations and ignition enhancement by NPHFD are explored. The optimal condition for plasma assisted ignition is discussed.

2. Numerical model and methods

2.1. One-dimensional (1-D) modeling for the critical ignition radius and the minimum ignition energy

To explore the effects of H_2 blending on NH_3 ignition, the ignition kernel development by a hot spot in various mixtures (NH_3/air, NH_3/H_2/air, H_2/air) are simulated using a one-dimensional (1-D) in-house code ASURF+ [38-43]. The detailed methodologies, numerical schemes, and validation of ASURF+ have been described in references [44-47]. In the simulations, the mixture is ignited at the center by a hot spot, shown by Eq. (1) The resulting spherical flame kernel propagates outwardly. The conservation equations for unsteady, compressible, multi-component reactive flow are solved using the finite volume method. The third-order weighted essentially non-oscillatory (WENO) scheme and the central difference scheme, respectively, are applied for convection and diffusion terms. Dynamic adaptive mesh refinement is used to ensure the finest mesh size of 7.8 μm near the flame front. Numerical convergence is validated by reducing the time step and mesh size.

The simulations are performed under fuel rich conditions with an equivalence ratio Φ of 1.2, an initial temperature of 700 K, a pressure of 1 atm, and zero flow velocity. For the NH_3/H_2/air mixture, the ratio between NH_3 and H_2 is 7:3. This initial temperature is selected to reflect typical ammonia gas turbine fuel-rich operating conditions. The 1-D computational domain spans from 0 to 3 cm in spherical coordinates, which is sufficient to ensure that the flame propagation is not affected by the boundary. For the boundary conditions, the symmetry conditions and zero flow velocity conditions are applied at R

= 0 and 3 cm, respectively. To simulate the hot spot ignition process where energy is deposited around the center during a short period, the following source term is introduced in the energy equation (1)

$$q_{ig}(R,t) = \begin{cases} \frac{3Q}{4\pi {r_{ig}}^3 \tau_{ig}} \exp\left[-\frac{\pi}{4}\left(\frac{R}{r_{ig}}\right)^6\right] & if\ t < \tau_{ig} \\ 0 & if\ t \geq \tau_{ig} \end{cases} \quad (1)$$

where $q_{ig}(R,t)$ represents the deposited energy per unit volume and time at position R and time t, Q the total ignition energy deposited into the mixture, τ_{ig} the duration of energy deposition, and r_{ig} the ignition kernel radius. τ_{ig} and r_{ig} are fixed at 0.2 ms and 0.2 mm, respectively. Additional simulations varying τ_{ig} and r_{ig} are conducted. The primary conclusions remain consistent irrespective of these values.

A comprehensive $NH_3/H_2/O_2/N_2$ combustion mechanism developed by Thorsen et al. [48] with an O_3 sub-mechanism [49] is used in this simulation. This mechanism consists of 34 species and 230 reactions.

2.2. Two-dimensional (2-D) plasma assisted ignition and combustion modeling

The plasma modeling for this study is performed using the MARCS-PAC model developed at Princeton University [28, 37, 50, 51]. This solver integrates the 2-D plasma solver PASSKEy [52-54] and the adaptive simulation of unsteady reactive 2-D flow solver ASURF+ [38, 41-43]. The drift-diffusion-reaction equations for plasma species, Helmholtz equations for photoionization, Poisson equation for electric fields, energy conservation equation for plasma discharge and electrons, and unsteady, multi-component, reactive, compressible Navier–Stokes (N-S) equations are solved by time-splitting solution methods. Detailed descriptions of the governing equations and numerical schemes are provided in Ref. [28].

In this work, simulations are carried out in fuel-rich NH_3/H_2/air (0.190 NH_3/0.082 H_2/0.153 O_2/0.575 N_2) mixtures with a 7:3 ratio of NH_3 to H_2, at an equivalence ratio of 1.2, 700 K, and 1 atm (the effective Lewis number *L*e is 1.44). Note that for NH_3/H_2/air flames, operating under rich conditions helps reduce NO_x production via the NO_x reburning mechanism. An equivalence ratio of 1.2 is typically employed in the first stage of gas turbine combustion to minimize NO_x emissions. The selected temperature mimics typical gas turbine conditions, while the pressure is chosen to establish a baseline for investigating the non-equilibrium energy transfer processes induced by NSD. Additionally, this pressure facilitates meaningful comparisons with previous studies [28-32, 37] in the field, even though practical gas turbines usually operate at higher pressures. To initiate the discharge, a uniform pre-ionized mixture with a low initial electron number density of 10^4 cm^{-3} is used [55]. The initial ion densities are set to ensure quasi-neutrality. A nanosecond discharge with a single pulse is used to study the effects of the applied voltage and the electrode gap size, while NPHFD is used to study the effects of the pulse repetition frequency and pulse number. For each pulse, a trapezoidal waveform voltage with a peak value

ranging from 1.5 to 5.0 kV and with a rise time of 2 ns is applied to the electrodes. The discharge duration of each pulse is adjusted by maintaining a constant energy deposition in the plasma across all simulations.

An experimentally validated plasma-combustion kinetic model for $NH_3/O_2/N_2$ mixtures [15] is used. The original model incorporates 77 species and combines 894 reactions in the plasma kinetic sub-model with 230 reactions in the combustion kinetic sub-model. Detailed descriptions of this model can be found in [15, 22]. To save computational time while maintaining the accuracy, a reduced model is developed in the plasma kinetic sub-model. The combustion kinetic sub-model is not reduced due to the negligible impact on computational time. The reduced model has been validated by comparing species concentrations, temperature profiles, and ignition delay times under various conditions, as shown in Fig. S1 and S2, and Table S1 in the Supplementary Materials. Then, the H_2 plasma sub-model from [56] is incorporated. The plasma-combustion kinetic model for $NH_3/H_2/O_2/N_2$ mixtures in the 2-D simulations consists of 47 species and 71 reactions. It incorporates electronically excited species $O(^1D)$, N_2^* ($N_2(A)$, $N_2(B)$, $N_2(a')$, $N_2(C)$), $N(^2D)$; ions NH_3^+, NH_4^+, H_2^+, O_2^+, N_2^+, N_4^+, O^-, O_2^-; and electrons.

To reduce the complexity of 3-D plasma modeling and focus on the kinetic effects of plasma discharge on ignition, an axisymmetric needle-to-ring electrode configuration is used instead of the pin-to-pin configuration. Modeling a pin-to-pin plasma with flow requires a 3-D setup due to the vertical alignment of the electrode axis and flow direction, which is computationally prohibitive for plasma-assisted combustion with detailed chemistry. Despite differences from real pin-to-pin plasma experiments, the conclusions align well with experimental findings [29–31]. Fig. 1 illustrates the 2-D computational domain and geometry. The *R*-axis represents the electrode radius direction, and the *Z*-axis represents the length direction of the needle electrode and gas flow within the cylindrical coordinates. The computational domain is 3.5 mm × 15 mm, ensuring that the flow remains undisturbed by the vertical boundaries and the flame propagates sufficiently far to observe the ignition kernel development. Validation cases are conducted to ensure the suitability of the 3.5 mm radius, as shown in Fig. S3 in the Supplementary Materials. The results demonstrate that the size and shape of the ignition kernel remain identical for x-axis ranges of 3.5 mm and 5 mm. A flow is introduced from the bottom at a speed of v = 20 m/s, maintaining the same mixture, temperature, and pressure as the initial conditions. Non-reflective boundary conditions are employed for other external boundaries, symmetric boundary conditions are applied at the centerline, and reflective boundary conditions are applied at the center electrode.

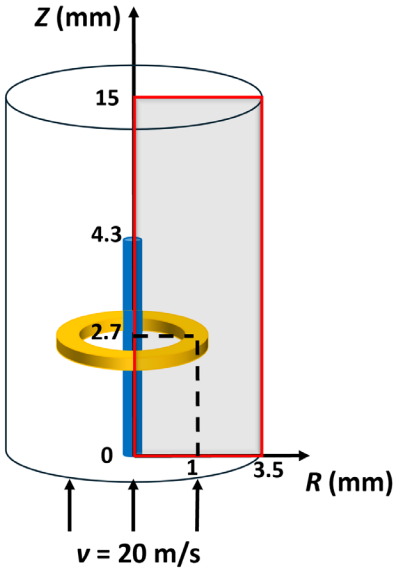

Fig. 1 2-D computational domain and geometry.

The needle electrode has a length of 4.3 mm. The gap size between the need and ring electrodes is 1 mm, unless specified otherwise. The ring electrode is positioned at Z = 2.7 mm, approximately midway along the needle electrode, to mitigate the high electric fields arising near the sharp edges of the electrodes. The radii of the needle and ring electrodes are set at 60 μm and 40 μm, respectively, which are small enough to reduce flow recirculation near the electrodes. To minimize computational expenses, a fine and uniform orthogonal mesh (10 μm × 10 μm) is used within the plasma discharge area, while a larger mesh size (40 μm × 40 μm) is set in the outer region. High voltage is applied to the ring electrode, and the needle electrode is grounded. The time step is determined by the shortest characteristic timescale of the drift dynamics of charged species, plasma kinetics, combustion kinetics, and fluid dynamics across all grids.

3. Results and discussion

3.1. Effects of H_2 blending on the critical ignition radius and ignition kernel development of NH_3

To enhance the reactivity of NH_3, the effect of H_2 blending on NH_3 ignition is investigated by calculating the critical ignition radius and the minimum ignition energy (MIE) using the 1-D simulation model. Fig. 2 shows the flame kernel propagation speed S_i as a function of flame radius for different mixtures and the variation of the critical ignition radius (R_c) at MIE for different mixtures. For the NH_3/H_2/air mixture, the ratio between NH_3 and H_2 is 7:3. MIE is determined through a trial-and-error process, achieving a relative error within 5%. The square in each case marks the critical ignition radius. In each case, the flame propagation speed first decreases and then increases with the flame radius, with the lowest point indicating the critical ignition radius. As the flame kernel radius increases sufficiently, S_i converges to the laminar flame speed. Successful ignition requires an initial ignition kernel (or MIE) that exceeds the critical ignition radius (or

critical ignition energy). A larger critical ignition radius implies greater difficulty or higher MIE in igniting the mixture. The simulated MIE values for different mixtures are as follows: NH_3/air at 4.0 mJ, H_2/air at 0.35 mJ, and NH_3/H_2/air at 0.7 mJ. The corresponding critical ignition radii are 0.098 cm for NH_3/air, 0.042 cm for H_2/air, and 0.049 cm for NH_3/H_2/air, respectively. It is seen that adding 30% H_2 significantly reduces both the MIE and the critical ignition radius, thus enhancing ignition.

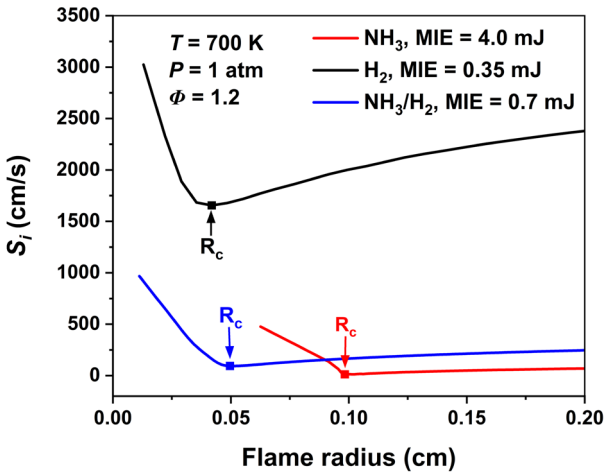

Fig. 2 Flame propagation speed S_l as a function of flame radius for different mixtures at the minimum ignition energy. The square in each case marks the critical ignition radius (R_c).

2-D plasma modeling is employed to investigate the dynamics of plasma-assisted ignition kernel development and propagation. Fig. 3 shows 2-D temperature distribution at selected times during plasma-assisted ignition for NH_3/H_2/air and NH_3/air mixtures. A single discharge pulse with energy of 0.4 mJ and the peak voltage of 5.0 kV is used in each case. In the case of the NH_3/air mixture, the initial ignition kernel generated by plasma fails to lead to successful ignition due to convective heat loss and radical quenching driven by fluid motion. However, with a 30% addition of H_2, the ignition kernel volume continues to grow, facilitated by the reduced critical ignition radius (Fig. 2). This confirms the effectiveness of H_2 blending in enhancing NH_3 ignition in flowing mixtures. In the following sessions, the 0.190 NH_3/0.082 H_2/0.153 O_2/0.575 N_2 mixture is used to study the control of non-equilibrium excitation and efficient ignition.

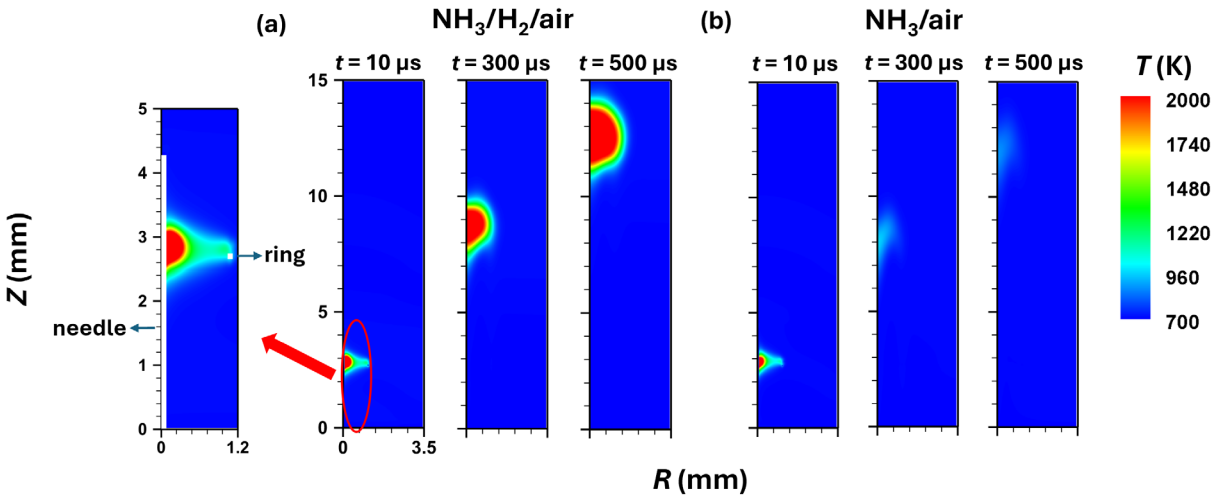

Fig. 3 2-D temperature distributions at selected times during plasma-assisted ignition for (a) NH_3/H_2/air and (b) NH_3/air mixtures. The needle and ring electrode positions are marked in the zoomed-in figure.

3.2. Effects of plasma voltage on ignition enhancement

In this section, the impacts of discharge voltage (U) on plasma-assisted ignition enhancement are explored. Attention is focused on how the reduced electric field E/N (ratio of electric field and gas number density) controls non-equilibrium energy transfer. The applied peak pulse voltage ranges from 1.5 to 5.0 kV with the same discharge energy of 0.4 mJ. Fig. 4 shows the time evolutions of the ignition kernel volume under different applied voltages. The ignition kernel volume is defined as the integrated volume where the temperature exceeds 2000 K, nearing the flame front. In each case, the generated ignition kernel continually grows with time. At U = 2.0 kV, the most efficient ignition enhancement is observed, marked by the largest ignition kernel volume at t = 0.3 ms. At U = 5.0 kV, the ignition kernel volume at t = 0.3 ms is 15.3% smaller compared to the value of U = 2.0 kV.

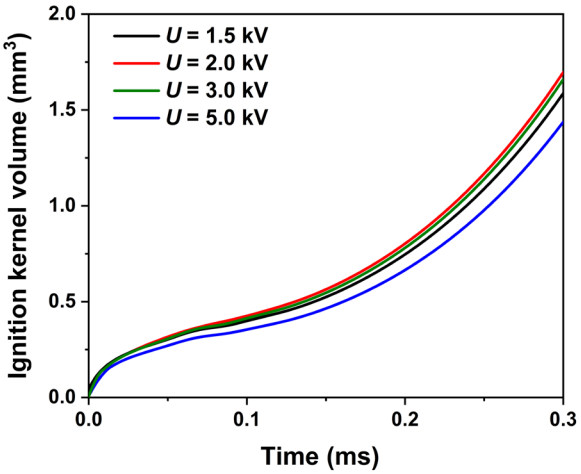

Fig. 4 Time evolutions of the ignition kernel volume under different applied voltages at the discharge energy of 0.4 mJ.

To understand the non-equilibrium energy transfer and its effects on ignition enhancement, Fig. 5 shows the distribution of electron energy into various excitation modes as a function of *E/N* in the 0.190 NH_3/0.082 H_2/0.153 O_2/0.575 N_2 mixture computed by BOLSIG+ [57]. Below 10 Td, electron energy is primarily deposited into rotational and NH_3 vibrational excitation modes. As *E/N* increases, N_2 vibrational excitation becomes the primary pathway of electron energy deposition, although some energy is also allocated to the vibrational excitation of H_2 and O_2. As the NH_3 rotational and vibrational excitation decreases, the energy deposition into NH_3 and O_2 dissociation and N_2 electronic excitation grows. Between 100 and 300 Td, the dissociation of NH_3, H_2, O_2, and N_2, along with the electronic excitation of N_2, becomes dominant in the energy transfer process. A further increase in *E/N* significantly enhances ionization pathways. Fig. 6 shows the time evolution of the reduced electric field at the center of the discharge gap (R = 0.5 mm, Z = 2.75 mm). The initial 2 ns represents the voltage rise period at U = 1.5 and 2.0 kV, during which the reduced electric field gradually increases. After this period, breakdown occurs, leading to a sudden rise in the *E/N*, which then stabilizes into a plateau. At U = 3.0 and 5.0 kV, the voltage rise period is shorter for the given energy deposit, and the breakdown occurs earlier but ignition kernel development is slower. An applied voltage of 2.0 kV corresponds to an *E/N* of approximately 200 Td during the plateau stage, which lasts until 10 ns. This suggests that an *E/N* of around 200 Td is optimal for ignition enhancement. This conclusion aligns with the findings in [22], which indicates that the production of electronically excited species and radicals is most efficient in reducing ignition delay time.

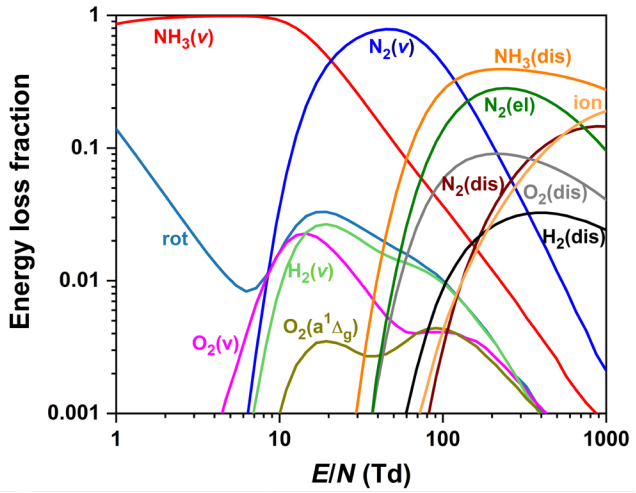

Fig. 5 Fractions of electron energy deposition into different excitation modes as a function of *E/N* in the 0.190 NH_3/0.082 H_2/0.153 O_2/0.575 N_2 mixture. (rot: rotational excitation; *v*: vibrational excitation; el: electronic excitation; dis: dissociation; ion: ionization)

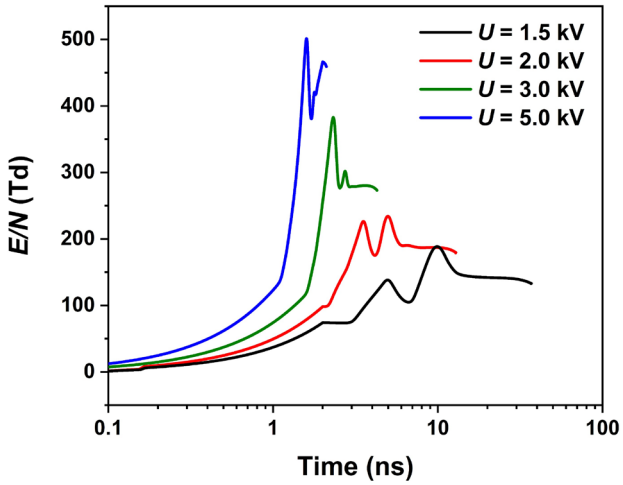

Fig. 6 Time evolution of the reduced electric field at the center of the discharge gap (R = 0.5 mm, Z = 2.75 mm).

Fig. 7(a)-(h) shows the time evolutions of the mole fractions of various species at R = 0.5 mm and Z = 2.75 mm. Initially (when $t < 10^{-7}$ s), excited species such as $N_2(B)$ and $O(^1D)$ are generated, followed by the production of radicals such as NH_2, OH, O, and H, along with the consumption of NH_3. Two distinct stages of NH_3 consumption can be observed from Fig. 7(a): an initial phase from 10^{-9} to 10^{-7} s driven by electron impact reactions, leading to the generation of excited species and radicals, and a subsequent phase from 10^{-7} to 10^{-5} s characterized by radical consumption/propagation and NH_3 oxidation. NH_3 is most effectively consumed at U = 2.0 kV because of the efficient energy coupling. By the end of the second phase, most of the NH_3 in the initial ignition kernel should be consumed. However, the 20 m/s flow from the bottom causes the ignition kernel to shift by 0.2 mm by 10^{-5} s. As a result, the mole fraction of NH_3 at the observed location eventually returns to its original value due to the movement of the ignition kernel with the flow. At U = 2.0 kV, the generation of the NH_2 radical is most efficient through the reactions $e + NH_3 \rightarrow e + NH_2 + H$ and $N_2^* + NH_3 \rightarrow N_2 + NH_2 + H$. This is because NH_3 dissociation is optimized within an E/N range of 100-200 Td, as shown in Fig. 5. The OH radical, crucial for chain-branching and chain-propagation in NH_3 and H_2 oxidation, is also generated most efficiently at U = 2.0 kV shown in Fig. 7(c) through reactions $NH_3 + O = NH_2 + OH$ and $H_2 + O = OH + H$. Similarly, the production of the O radical peaks at U = 2.0 kV through reactions $e + O_2 \rightarrow e + O + O/O(^1D)$ and $N_2^* + O_2 \rightarrow N_2 + O + O/O(^1D)$, which are most active at an E/N of approximately 200 Td shown in Fig. 7(d). The generation of H radicals is also most efficient at U = 2.0 kV, initially produced via the reaction $e + H_2 \rightarrow e + H + H$ and $e + NH_3 \rightarrow e + NH_2 + H$. Subsequently, the mole fraction of H continues increasing until 10^{-7} s through reactions such as $N_2^* + H_2 \rightarrow N_2 + H + H$ and $H_2 + O = OH + H$. The excited species including $O(^1D)$ and $N_2(B)$ are also produced effectively at U = 2.0 kV, respectively, via $e + O_2 \rightarrow e + O + O(^1D)$ and $e + N_2 \rightarrow e + N_2(B)$, as the reduced electric field of 200-300 Td promotes electron energy deposition into electronic excitation and dissociation. These excited species significantly accelerate radical generation via

$NH_3 + O(^1D) \rightarrow NH_2 + OH$, $H_2 + O(^1D) \rightarrow OH + H$, $N_2(B) + NH_3 \rightarrow N_2 + NH_2 + H$, and $N_2(B) + O_2 \rightarrow N_2 + O + O$. At higher voltages ($U$ = 5.0 kV), ion species, including NH_3^+, H_2^+, O_2^+, N_2^+, NH_4^+, and N_4^+, are generated more efficiently, as indicated in Fig. 5 and Fig. 7(h). However, this increased ion generation consumes significant electron energy, promotes thermalization, thus negatively impacting radical generation and ignition performance. Conversely, at lower voltages (U = 1.5 kV), the dissociation of NH_3, H_2, O_2, and N_2, as well as the electronic excitation of N_2, becomes less prominent. Specifically, insufficient electron energy is deposited into the generation of excited species, such as $O(^1D)$ and $N_2(B)$, as shown in Fig. 7. This, in turn, affects radical generation and ammonia oxidation. For example, the mole fractions of OH, O, and H radicals are lower compared to those at U = 2.0 kV, resulting in less effective ammonia consumption at U = 1.5 kV. In conclusion, the generation of most radicals and electronically excited species is most effective at U = 2.0 kV, explaining the optimal ignition performance observed in Fig. 4.

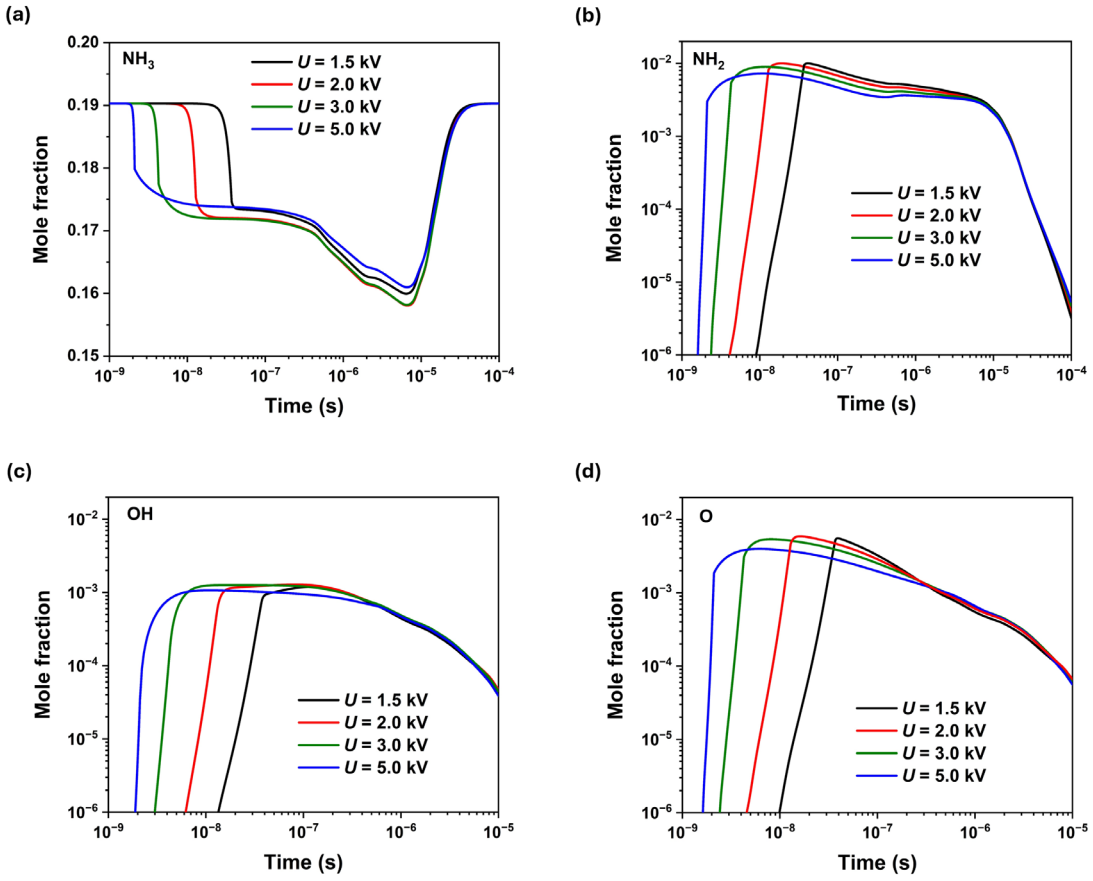

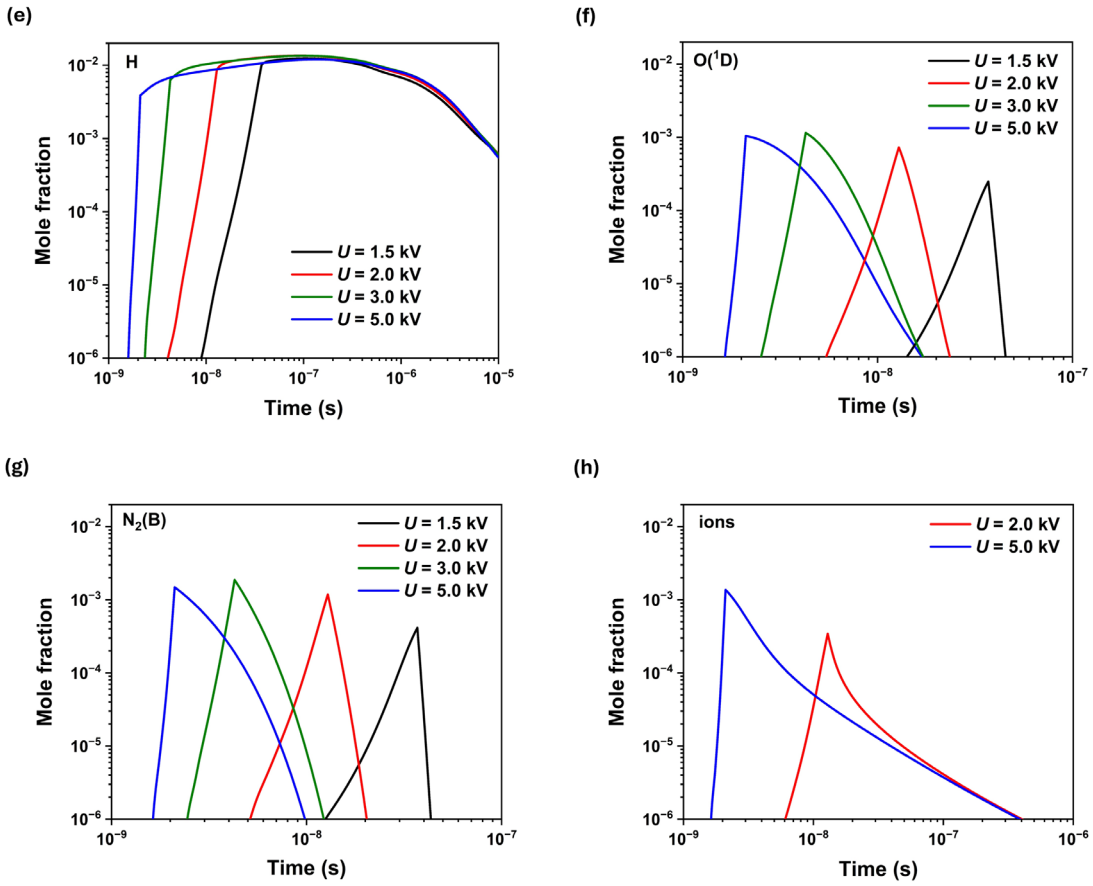

Fig. 7 Time evolutions of the mole fractions of (a) NH_3, (b) NH_2, (c) OH, (d) O, (e) H, (f) $O(^1D)$, (g) $N_2(B)$, (h) summarization of ions at the center of the discharge gap (R = 0.5 mm, Z = 2.75 mm).

3.3. Effects of electrode gap size on ignition enhancement

In previous research of hydrogen ignition [28], the electrode gap size has been shown to significantly influence the spatial discharge energy distribution. In this section, plasma-assisted NH_3/H_2/air ignition with varying electrode gap sizes (D), ranging from 0.35 to 0.8 mm, is explored while maintaining a constant applied voltage of 5.0 kV and discharge energy of 0.2 mJ.

Fig. 8 presents the time evolutions of the ignition kernel volume with different electrode gap sizes. The results indicate a non-monotonic relationship between the ignition kernel volume and the electrode gap size, with optimal ignition enhancement observed at D = 0.50 mm. An excessively large electrode gap can lead to ignition failure due to the large critical ignition radius. This phenomenon is further elucidated in Fig. 9, which shows the 2-D temperature distribution at selected times under various electrode gap sizes. For gap sizes of D = 0.35 and 0.50 mm, the ignition kernel develops rapidly. However, at D = 0.80 mm, the larger discharge region results in a lower discharge energy density. This reduction

in energy density combined with heat loss and quenching effects lowers the radical production rate and prevents the initial ignition kernel from reaching the critical volume necessary for sustained ignition, ultimately leading to ignition failure.

The electrode gap size also influences the *E/N* values (shown in Fig. S4 in the Supplementary Materials), which in turn affects species production in the discharge. As discussed in Section 3.2, at U = 5.0 kV and D = 1.0 mm, the *E/N* exceeds the optimal value. Further reducing the electrode gap size below 0.8 mm would cause the *E/N* to deviate even more from the optimal range, thereby negatively impacting ignition performance. Based on observations, the effects of *E/N* are less significant compared to the discharge energy density. To validate this, Fig. S5 shows the time evolution of the ignition kernel volume for different electrode gap sizes at a discharge energy of 0.2 mJ, with the same average *E/N* values in the discharge region. The applied voltage is 5.0 kV for the 0.80 mm gap size and is adjusted accordingly for 0.35 mm at 2.187 kV, 0.5 mm at 3.125 kV and 0.6 mm at 3.75 kV, respectively. The conclusion remains consistent with the findings above.

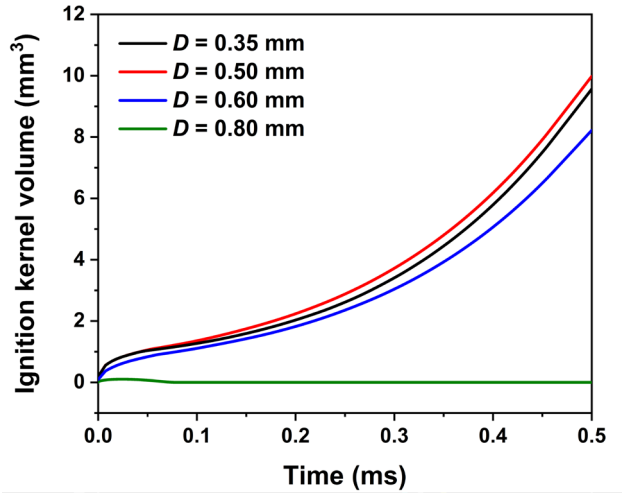

Fig. 8 Time evolutions of the ignition kernel volume with different electrode gap sizes at the discharge energy of 0.2 mJ.

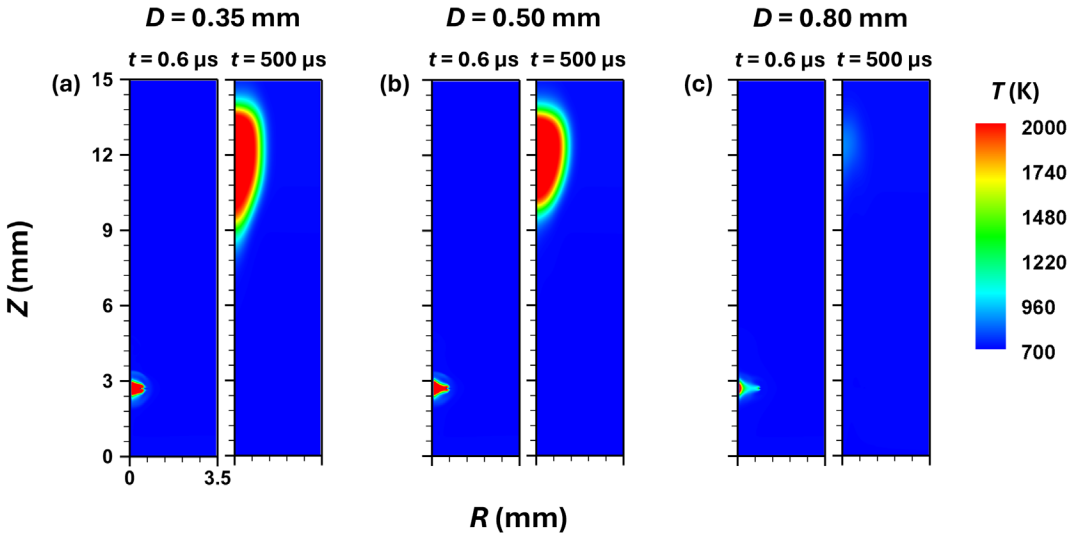

Fig. 9 2-D temperature distribution at t = 0.6 μs and 500 μs with D = (a) 0.35, (b) 0.50, and (c) 0.80 mm.

Fig. 10 shows the distributions of temperature and the mole fractions of electron, O, OH, O(^{1}D), and NH_3 along the *R*-axis direction at t = 150 ns and Z = 2.75 mm. The findings reveal a consistent pattern where the highest concentrations of electron, O, OH, O(^{1}D), and temperature occur near the needle, are moderately high near the ring and drop to their lowest mid-way between these points. This distribution pattern indicates that a smaller electrode gap size elevates the concentration of active species and temperature within the discharge region. For an effective ignition threshold set at 2000 K, the most efficient ignition occurs at D = 0.50 mm, where the temperature across the entire discharge region consistently exceeds this threshold, maximizing the ignition kernel area. In contrast, for D = 0.80 mm, effective ignition is confined to a small area near the needle. The highest reduced electric field and most concentrated energy deposition with D = 0.35 mm result in the highest electron number density and radical mole fractions. However, the narrower discharge region limits the ignition kernel area compared to that at D = 0.50 mm, which will be discussed later. Fig. 10(d) and (f) reveal that the OH mole fraction near the needle is lower than in the middle, indicating that OH is being consumed during the oxidation of NH_3, which is nearly depleted near the needle. This suggests that the OH radicals are actively participating in the chemical reactions involved in NH_3 oxidation.

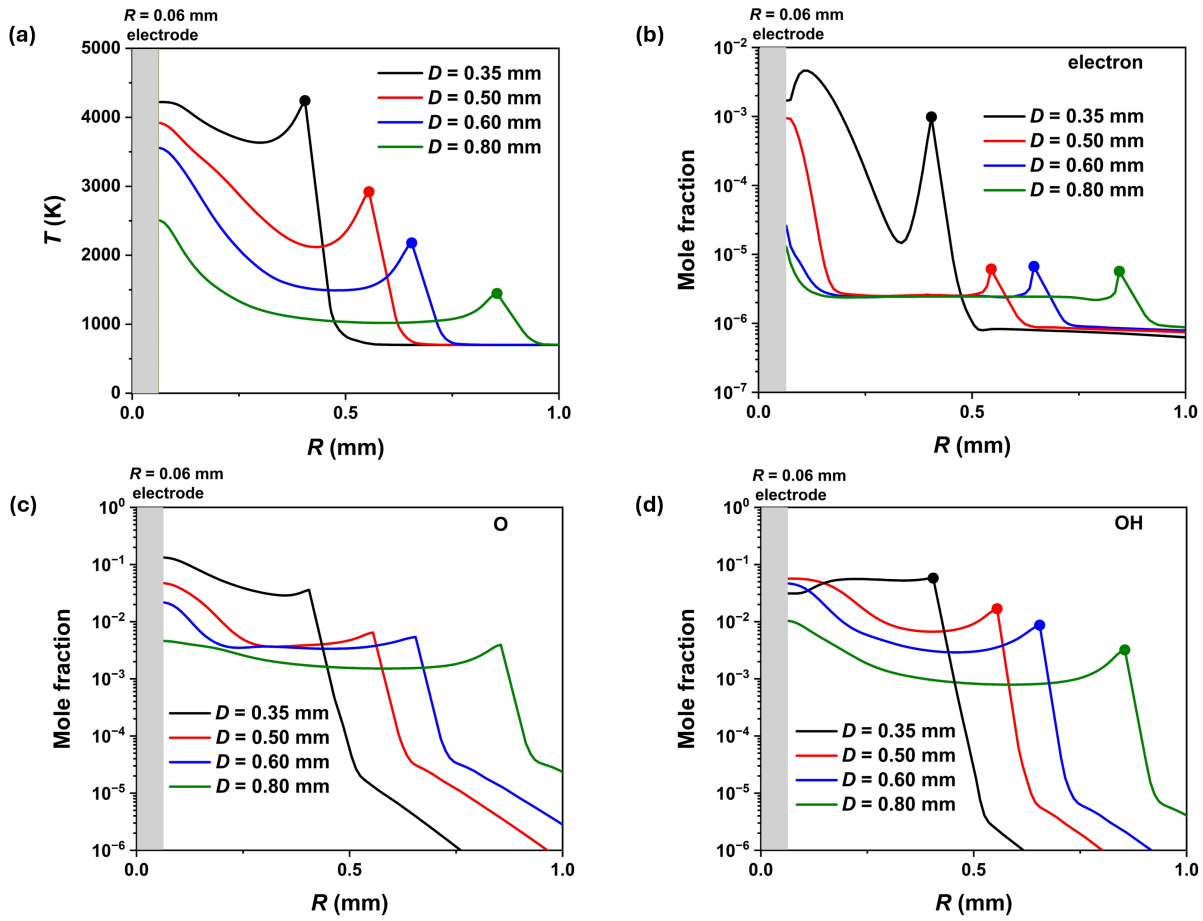

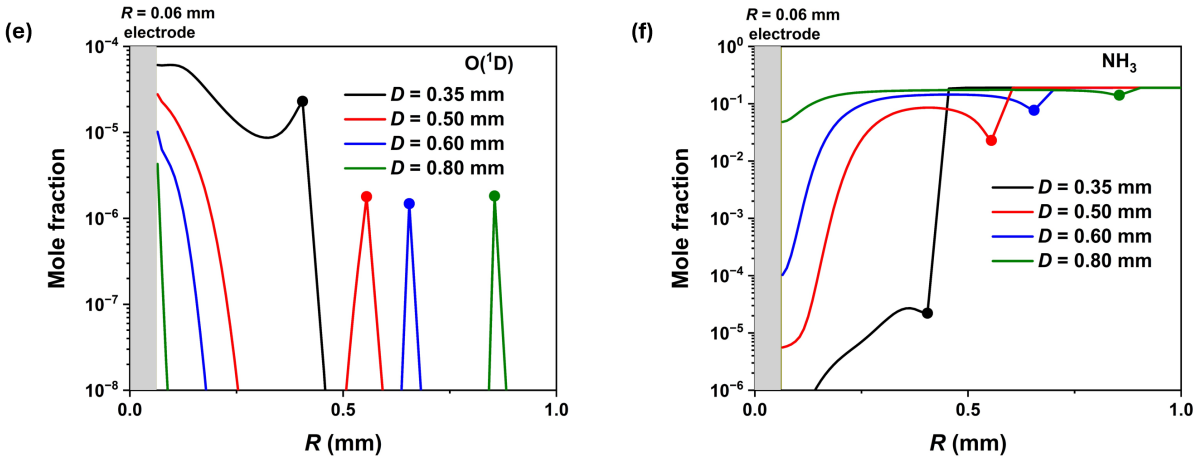

Fig. 10 Distributions of (a) temperature and the mole fractions of (b) electron, (c) O, (d) OH, (e) O(^{1}D), and (f) NH_3 along the R-axis direction at t = 150 ns and Z = 2.75 mm across different electrode gap sizes. The gray region indicates the needle electrode, and the circular dots indicate the ring electrode.

Although the mole fractions of active species are the most at t = 150 ns with D = 0.35 mm, the ignition kernel development with the flame propagation is not as effective as D = 0.5 mm. To explain this, the flame propagation speed S_i as a function of the ignition kernel volume is illustrated in Fig. 11. The S_i values are determined based on the Z position with the maximum heat release at R = 60 μm. As shown in Fig. 10(a), the initial ignition kernel at D = 0.50 mm is the largest. Consequently, a larger flame surface area at this gap size leads to increased fuel consumption and, thereby, a higher flame propagation speed compared to D = 0.35 mm. This effect can also be analyzed from the perspective of flame stretch. According to the linear model (LM) for normalized flame propagation speed $V = S_i/S_i^0$ in [38] (where S_i^0 is the unstretched flame propagation speed),

$$V = 1 - Ma \cdot Ka, \tag{2}$$

where $Ma = Le^{-1} - (Z/2)(Le^{-1} - 1)$ is the Markstein number, $Ka = K\delta/S_u^0$ the Karlovitz number, Z the Zel'dovich number, K the flame stretch rate, δ the flame thickness of an adiabatic planar flame, and S_u^0 the unstretched laminar flame speed with respect to the unburned mixture. Equation (2) describes how the flame propagation speed deviates from its unstretched value in response to flame stretch. With a larger flame stretch rate, the deviation of the flame propagation speed from its unstretched value increases. For the specific scenario under consideration, where the Lewis number is over unity and thus the Markstein number is a positive value, the flame propagation speed is reduced relative to its unstretched value.

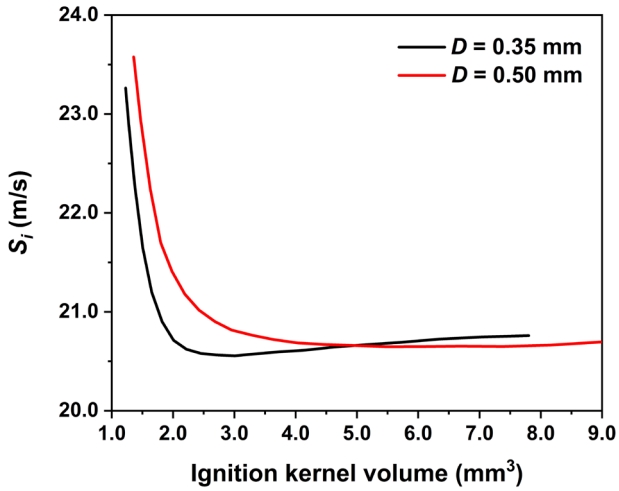

Fig. 11 Flame propagation speed S_i as a function of the ignition kernel volume with D = 0.35 and 0.50 mm.

The flame regions shown in Fig. 9(a) and (b) have two principal radii of curvature, R_1 and R_2, oriented such that they point away from the flame surface towards the center of curvature. According to [58], the flame stretch rate can thus be expressed as

$$K = \left(\frac{1}{R_1} + \frac{1}{R_2}\right)\frac{dR_f}{dt}, \tag{2}$$

where R_f is the instantaneous flame radius. Fig. 9(a) shows that the flame region with D = 0.35 mm is thin and elongated, with one principal radius of curvature significantly smaller than the other one. In contrast, Fig. 9(b) indicates that at D = 0.5 mm, the two principal radii are more similar, giving the flame a more spherical shape. Therefore, the flame stretch rate is larger with a larger $\frac{1}{R_1} + \frac{1}{R_2}$ at D = 0.35 mm, leading to a greater initial deviation in the flame propagation speed from the unstretched value. This explains why, with D = 0.35 mm, the flame propagation speed is initially lower when the ignition kernel starts to grow. The lower flame propagation speed, in turn, delays the growth of the ignition kernel, which accounts for the difference of the ignition performance with D = 0.35 and 0.50 mm. It is noted that as the flame propagates a sufficient distance, the flame propagation speed becomes consistent across different cases. However, in Fig. 11, the flame propagation speed at the end still deviates between the two cases because the flame has not yet propagated far enough. This indicates that the flame shape, whether more elongated or spherical, continues to influence the propagation.

It is noted that heat loss to the electrodes is not considered in this work. However, in our previous study [28], the effects of electrode diameter and gap size in the pin-to-pin configuration for H_2/air ignition assisted by NSD were investigated by comparing cases with and without heat loss. While the specific conditions and plasma configuration differ, the findings are relevant here. For smaller electrode sizes, the impact of heat loss on the ignition kernel volume becomes less significant. For instance, with a 1.0 mm electrode diameter in the pin-to-pin configuration, the difference in ignition kernel volume is less than 10%. In this work, the needle and ring electrode radii are 60 μm and 40 μm, respectively, which are small enough

to neglect heat loss effects. While smaller electrode gap sizes increase the influence of heat loss, the impact remains manageable. If heat loss were considered, the ignition kernel volume for D = 0.35 mm would decrease slightly. However, the non-monotonic dependence of ignition kernel volume on gap size would still be observed, with the optimal gap size shifting slightly larger.

3.4. Effects of pulse repetition frequency on ignition enhancement

To study the synergistic effects of multiple discharge pulses on ignition, two sequential pulses with the same discharge energy but with different pulse repetition frequencies (f) are examined. The discharge energy per pulse is set to 0.2 mJ, with an applied voltage of 5.0 kV and an electrode gap size of 1.0 mm. Note that a single pulse of 0.2 mJ fails to ignite the mixture. Fig. 12 shows the ignition kernel volume at different pulse repetition frequencies, with dashed lines representing the ignition kernel volume for a single pulse of 0.4 mJ. To illustrate the ignition kernel development process, two time points, t = 0.3 ms and t = 0.5 ms, are selected. At lower pulse frequencies, ignition enhancement is less effective compared to using a single pulse. This reduced efficacy is attributed to the radical quenching and heat loss during the inter-pulse period. However, using a pulse repetition frequency greater than 100 kHz significantly enhances ignition. The optimal pulse repetition frequency is found to be 500 kHz, with the increase in ignition kernel volume of 98.7% at t = 0.3 ms and 68.4% at t = 0.5 ms compared to the single-pulse case. Beyond this frequency, further increases lead to a reduction in ignition kernel volume. As pulse repetition frequency approaches infinity, two sequential pulses merge to resemble that of a single pulse, thereby aligning the ignition performance with that observed for a single pulse of 0.4 mJ.

Fig. 13 shows 2-D temperature distribution at selected times for f = (a) 50 kHz, (b) 500 kHz, and (c) 10 MHz. The first image in each frequency corresponds to the time when the second pulse starts, and the second image corresponds to the time when the second pulse ends. In Fig. 13(a), the discharge energy is dispersed by the time the second pulse ends, as the second pulse does not fully coincide with the first pulse. As a result, the ignition kernel at 100 μs and 500 μs is smaller. In Fig. 13(b), the discharge energy is more focused, resulting in the largest ignition kernel. This is because the second pulse coincides with the existing ignition kernel, enhancing radical accumulation and energy deposition. In Fig. 13(c), the second pulse occurs immediately after the first pulse ends, leaving insufficient time for pressure wave relaxation and radical accumulation enhancement, which will be discussed later. Consequently, by the time the second pulse ends, the ignition kernel is smaller compared to the case with f = 500 kHz.

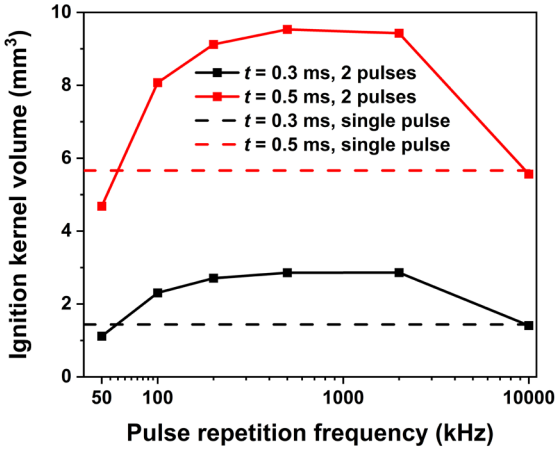

Fig. 12 Ignition kernel volume with different pulse repetition frequencies at t = 0.3 and 0.5 ms. In cases with 2 pulses, the discharge energy per pulse is 0.2 mJ. The dashed lines mark the ignition kernel volume for a single pulse of 0.4 mJ.

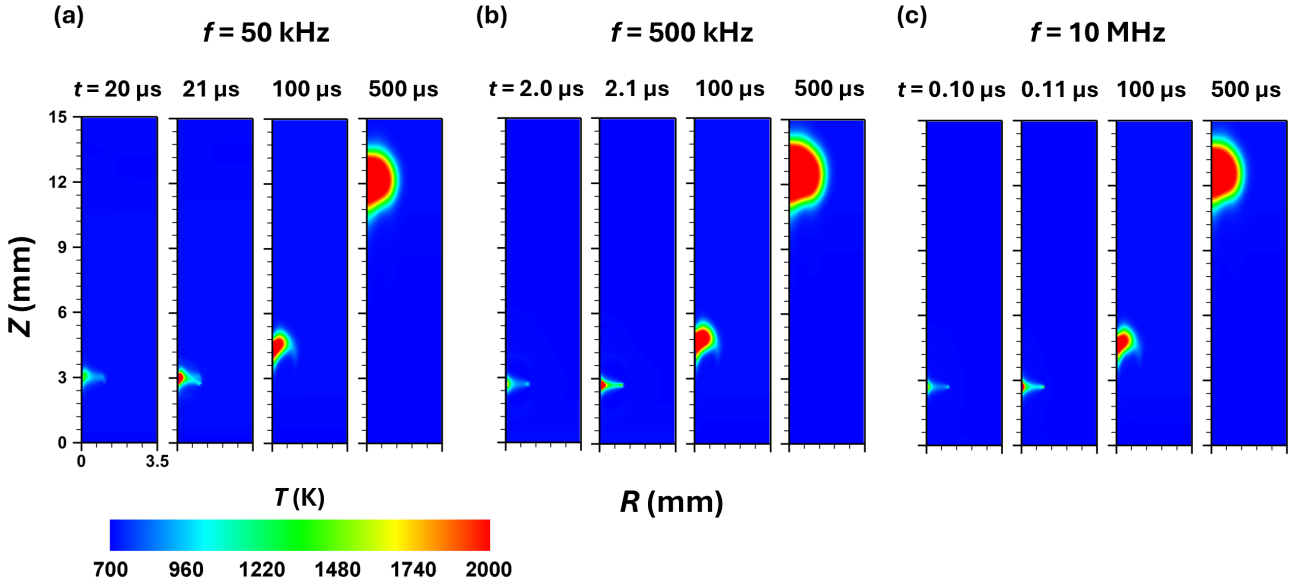

Fig. 13 2-D temperature distribution at selected times for f = (a) 50 kHz, (b) 500 kHz, and (c) 10 MHz. The first image in each part corresponds to the time when the second pulse starts, and the second image corresponds to the time when the second pulse ends.

To elucidate the non-monotonic relationship between the ignition kernel volume and pulse repetition frequency, Fig. 14 presents time evolutions of (a) OH mole fraction, (b) temperature, and (c) pressure at a fixed position (R = 0.5mm, Z = 2.75 mm) using a single pulse and 2 pulses with different pulse repetition frequencies. For a single pulse, the OH mole fraction peaks at 1.1×10^{-3} at the end of the first pulse around $t = 10^{-8}$ s, and the temperature reaches a maximum of nearly 1200 K around $t = 10^{-5}$ s. With two pulses, both the OH mole fraction and temperature decrease after the first pulse due to the divided pulse discharge energy. At f = 10 MHz, the OH mole fraction and temperature eventually reach values comparable to those observed with a single pulse, suggesting that at very high frequencies, the effect of using two pulses

mimics that of using one single pulse. At f = 500 kHz, there is a significant increase in both the OH mole fraction and temperature at the second peak, as the timing of the second pulse coincides with the existing ignition kernel. This overlap effectively pumps radicals and accelerates OH accumulation, resulting in a larger ignition kernel. Conversely, at f = 50 kHz, the temperature decreases due to heat loss before the second pulse starts, and the OH mole fraction diminishes, indicating radical quenching. The second peaks of OH mole fraction and temperature do not reach the heights seen with a single pulse.

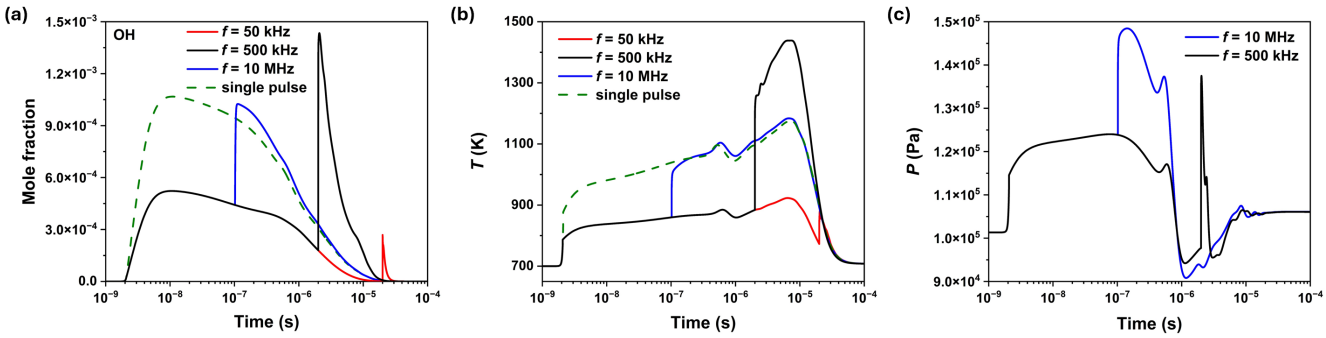

Fig. 14 Time evolutions of (a) OH mole fraction, (b) temperature, and (c) pressure at the fixed position R = 0.5 mm and Z = 2.75 mm using a single pulse and 2 pulses with different pulse repetition frequencies (f).

Further clarifying the differences between f = 10 MHz and f = 500 kHz, Fig. 14(c) shows that the pressure increases after the first pulse due to the pressure wave generated by the initial ignition kernel and then returns to its initial value before the second pulse begins at f = 500 kHz. According to the ideal gas law, with the temperature increase and pressure reverting to normal, the gas number density decreases. This reduction leads to an increase in the reduced electric field after the onset of the second pulse, which in turn increases the energy density and enhances the electron mole fraction as well as stimulates further radical generation. However, at f = 10 MHz, the pressure wave persists when the second pulse starts. With the concurrent increase in pressure and temperature, the number density remains stable, resulting in no change in the reduced electric field.

The NO mole fractions using a single pulse and 2 pulses with different pulse repetition frequencies are plotted in Fig. S6 in the Supplementary Materials. The results show that pulse repetition frequency has minimal impacts on NO formation. The effects of plasma on NO_x reduction are highly intricate and require further investigation in future work.

3.5. Effects of pulse number on ignition enhancement

Fig. 15 shows the ignition kernel volume with the same total discharge energy distributed across different numbers of pulses and pulse repetition frequencies at t = 0.5 ms. In all cases, the applied voltage is 5.0 kV, and the electrode gap size is 1.0 mm. At f = 50 kHz, the ignition enhancement is less effective compared to a single pulse case, regardless of the

number of plasma pulses used. Splitting the energy into more pulses at this frequency leads to ignition failure. At f = 100 kHz, ignition successfully initiates with 2 and 4 pulses but fails with 8 pulses. The optimal ignition performance occurs with 2 pulses. At f = 200 and 500 kHz, using 4 pulses results in the largest ignition kernel volume, 62.8% and 106.1% larger than that of a single pulse, respectively. The ignition kernel volume increases significantly by 105.2% with n = 8 from f = 200 to 500 kHz. As the frequency increases, the optimal pulse number also increases because more pulses maximize the overlap region and enhance the proliferation of radicals.

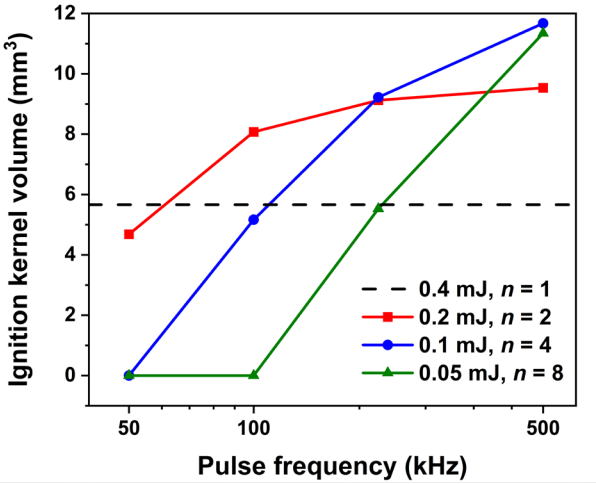

Fig. 15 Ignition kernel volume with the same total discharge energy of 0.4 mJ with different pulse numbers (n) and pulse repetition frequencies at t = 0.5 ms. The dashed line marks the ignition kernel volume for a single pulse of 0.4 mJ at t = 0.5 ms.

Fig. 16 sheds light on this phenomenon by displaying the time evolutions of OH mole fraction for different plasma pulse numbers at pulse frequencies of (a) 100 kHz, (b) 200 kHz, and (c) 500 kHz. With a single pulse, the OH mole fraction peaks above 10^{-3} when the first pulse ends around t = 10^{-8} s. For effective ignition enhancement using multiple pulses, a significant increase in peak OH mole fraction or maintaining a relatively high OH mole fraction for extended periods is necessary. At f = 100 kHz, the OH mole fraction decreases to about 10^{-5} when the second pulse starts. Only using two pulses reaches a similar peak value as a single pulse. With 4 pulses, the peak values decrease with increasing pulse number. Using 8 pulses results in a slight increase in the OH mole fraction during the later pulses, but the peak values are an order of magnitude lower than with a single pulse. At f = 200 kHz, the OH mole fraction is on the order of 10^{-4} when the second pulse starts. Using 2 pulses achieves a higher peak value than a single pulse. When 4 pulses are applied, all peak values are above 10^{-4}, with the first two peaks close to that of a single pulse. Therefore, significant ignition enhancement with 2 and 4 pulses is observed in Fig. 15. However, with 8 pulses, the peak OH mole fraction progressively decreases to around 10^{-5}. At f = 500 kHz, the best ignition performance is achieved with 4 pulses, indicated by the continuously increasing OH

mole fraction. The OH mole fraction at the fourth pulse is the highest, even exceeding the second peak of using 2 pulses. This suggests that continuous accumulation of radicals with overlapping ignition regions is most effective with a larger number of pulses and more dispersed energy at a high pulse repetition frequency. With 8 pulses, all peak values remain above 10^{-4}, with relatively high OH mole fractions sustained for an extended period, making it as effective as using 4 pulses.

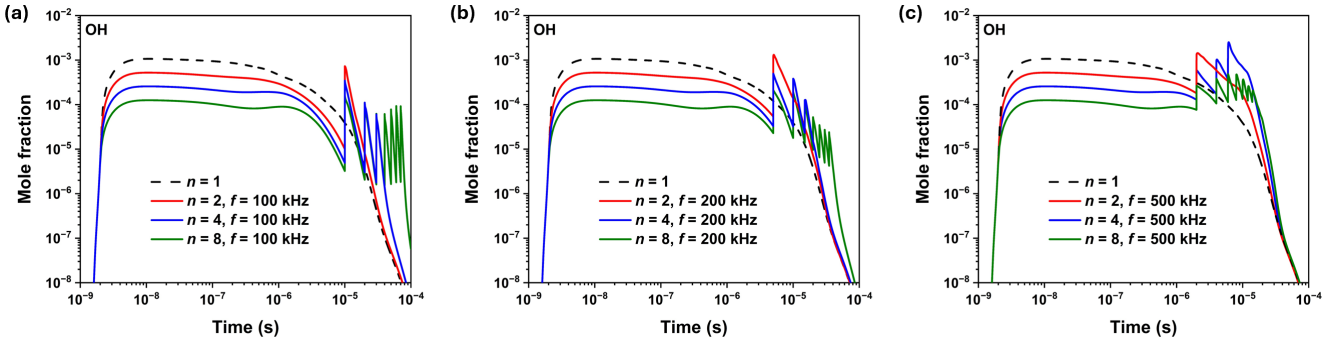

Fig. 16 Time evolutions of OH mole fraction at the fixed position R = 0.5 mm and Z = 2.75 mm using different pulse numbers at pulse frequencies of (a) 100 kHz, (b) 200 kHz, and (c) 500 kHz.

4. Conclusions

In this study, the effects of non-equilibrium energy transfer, plasma properties, and electrode gap distance on NH_3 ignition and flame propagation are investigated computationally using nanosecond discharges. 1-D flame propagation simulations reveal that adding 30% H_2 significantly reduces both the minimum ignition energy and the critical ignition radius, thus promoting ignition. 2-D plasma assisted ignition modeling shows that non-equilibrium energy transfer, applied voltages, electrode gap sizes, pulse repetition frequencies, and pulse numbers all affect ignition enhancement. Appropriate design of plasma discharge properties and mixture compositions is critical for ammonia ignition.

In summary, the result shows that there exists a non-monotonic dependence of the ignition kernel volume on the applied voltage. Specifically, an E/N of around 200 Td maximizes the ignition enhancement. Under this condition, the generation of radicals such as NH_2, H, O, and OH, along with electronically excited species such as $O(^1D)$ and $N_2(B)$, is most effective, facilitating efficient NH_3 consumption through enhanced radical production by electron impact reactions and the electronically excited species.

A non-monotonic relationship between the ignition kernel volume and the electrode gap size is also observed, with optimal ignition enhancement at a gap size of 0.5 mm. Excessively large electrode gaps lead to ignition failure due to reduced energy density coupled with heat loss and quenching effects. Conversely, an excessively small gap size constrains the size of the initial ignition kernel, which is less than the critical ignition radius. In addition, under this configuration the increase of the flame stretch leads to a reduced flame propagation speed.

Finally, it is also shown that the plasma pulse repetition frequency and pulse number with a fixed total discharge energy also affect the ignition enhancement in the nanosecond pulsed high frequency discharge. An optimal pulse repetition frequency of 500 kHz is identified, where a significant increase in both OH mole fraction and temperature at the second peak is observed. The coinciding overlap of the second pulse with the existing ignition kernel raises the reduced electric field, accelerates radical accumulation, and yields a larger ignition kernel. At lower frequencies, the ignition kernel volume decreases due to radicals quenching and heat loss during the inter-pulse period. At higher frequencies, the effect of two sequential pulses merges to resemble a single pulse, with an unchanged reduced electric field due to a simultaneous increase in pressure and temperature. Adjusting both pulse repetition frequency and number demonstrates that a higher frequency combined with more pulses maximizes the overlap region and significantly enhances ignition performance.

Acknowledgements

This work is supported by the DOE grant DE-SC0020233 of Plasma Science Center and the PPPL Plasma Science and Technology fellowship.

References

[1] United Nations, The Paris Agreement, 2015, available at http://unfccc.int/files/essential_background/convention/application/pdf/english_paris_agreement.pdf.

[2] A. Valera-Medina, H. Xiao, M. Owen-Jones, W.I. David, P. Bowen, Ammonia for power, Progress in Energy and combustion science 69 (2018) 63-102.

[3] H. Kobayashi, A. Hayakawa, K.K.A. Somarathne, E.C. Okafor, Science and technology of ammonia combustion, Proceedings of the Combustion Institute 37 (2019) 109-133.

[4] F. Chang, W. Gao, J. Guo, P. Chen, Emerging materials and methods toward ammonia‐based energy storage and conversion, Adv. Mater. 33 (2021) 2005721.

[5] J. Lim, C.A. Fernández, S.W. Lee, M.C. Hatzell, Ammonia and nitric acid demands for fertilizer use in 2050, ACS Energy Lett. 6 (2021) 3676-3685.

[6] F. Guo, C. Li, X. Xiu, K. Cheng, J. Qin, Comprehensive technical analyses of a solid oxide fuel cell turbine-less hybrid aircraft propulsion system using ammonia and methane as alternative fuels, Appl. Therm. Eng. 230 (2023) 120787.

[7] C. Lhuillier, P. Brequigny, F. Contino, C. Mounaïm Rousselle, Experimental study on ammonia/hydrogen/air combustion in spark ignition engine conditions, Fuel 269 (2020) 117448.

[8] S.W. Kim, A. Heckel, S. McKeen, G. Frost, E.Y. Hsie, M. Trainer, A. Richter, J. Burrows, S. Peckham, G. Grell, Satellite‐observed US power plant NO_x emission reductions and their impact on air quality, Geophys. Res. Lett. 33 (2006).

[9] X. Zhang, S. Moosakutty, R. Rajan, M. Younes, S. Sarathy, Combustion chemistry of ammonia/hydrogen mixtures: Jet-stirred reactor measurements and comprehensive kinetic modeling, Combust. Flame 234 (2021) 111653.

[10] M. Shahsavari, A. Konnov, X. Bai, A. Valera-Medina, T. Li, M. Jangi, Synergistic effects of nanosecond plasma discharge and hydrogen on ammonia combustion, Fuel 348 (2023) 128475.

[11] A. Alfazazi, E. Es-sebbar, X. Zhang, B. Dally, M. Abdullah, M. Younes, S. M. Sarathy, Counterflow flame extinction of ammonia and its blends with hydrogen and C1-C3 hydrocarbons, Applications in Energy and Combustion Science 12

(2022) 100099.
[12] S. O. Haputhanthri, T. T. Maxwell, J. Fleming, C. Austin, Ammonia and gasoline fuel blends for spark ignited internal combustion engines, Journal of Energy Resources Technology 137.6 (2015) 062201.
[13] X. Han, Z. Wang, M. Costa, Z. Sun, Y. He, K. Cen, Experimental and kinetic modeling study of laminar burning velocities of NH_3/air, NH_3/H_2/air, NH_3/CO/air and NH_3/CH_4/air premixed flames, Combust. Flame 206 (2019) 214-226.
[14] S. Shy, An experimental investigation on a flow-facilitated ignition at reduced and normal pressures for small, near-unity and large Lewis number of hydrogen/air and hydrogen/ammonia/air mixtures, Combust. Flame 270 (2024): 113746.
[15] H. Zhong, X. Mao, N. Liu, Z. Wang, T. Ombrello, Y. Ju, Understanding non-equilibrium N_2O/NO_x chemistry in plasma-assisted low-temperature NH3 oxidation, Combust. Flame 256 (2023) 112948.
[16] A. Bogaerts, E.C. Neyts, Plasma technology: an emerging technology for energy storage, ACS Energy Lett. 3 (2018) 1013-1027.
[17] Y. Ju, W. Sun, Plasma assisted combustion: Dynamics and chemistry, Progress in Energy and Combustion Science 48 (2015) 21-83.
[18] Y. Ju, J.K. Lefkowitz, C.B. Reuter, S.H. Won, X. Yang, S. Yang, W. Sun, Z. Jiang, Q. Chen, Plasma assisted low temperature combustion, Plasma Chemistry and Plasma Processing 36 (2016) 85-105.
[19] A. Starikovskiy, N. Aleksandrov, Plasma-assisted ignition and combustion, Progress in Energy and Combustion Science 39 (2013) 61-110.
[20] J. Choe, W. Sun, T. Ombrello, C. Carter, Plasma assisted ammonia combustion: Simultaneous NO_x reduction and flame enhancement, Combust. Flame 228 (2021) 430-432.
[21] S. Shy, V. T. Mai, Y. R. Chen, H. Y. Hsieh, Nanosecond repetitively pulsed discharges and conventional sparks of ammonia-air mixtures in a fan-stirred cruciform burner: Flammability limits and ignition transition, Applications in Energy and Combustion Science 15 (2023): 100164.
[22] X. Mao, H. Zhong, N. Liu, Z. Wang, Y. Ju, Ignition enhancement and NO_x formation of NH_3/air mixtures by non-equilibrium plasma discharge, Combust. Flame 259 (2024) 113140.
[23] R. Patel, C. Oommen, M. Thomas, Influence of reduced electric field (E/N) on plasma-assisted low-temperature oxidation, Journal of Propulsion and Power 36.2 (2020): 235-247.
[24] V. Smirnov, O. M. Stelmakh, V. I. Fabelinsky, D. N. Kozlov, A. M. Starik, N. S. Titova, On the influence of electronically excited oxygen molecules on combustion of hydrogen–oxygen mixture, Journal of Physics D: Applied Physics 41, no. 19 (2008): 192001.
[25] N. Liu, B. Mei, X. Mao, Z. Wang, Z. Sun, Y. Xu, Z. Shi, Y. Ju, Kinetics of low temperature plasma assisted NH_3/H_2 oxidation in a nanosecond-pulsed discharge, Proceedings of the Combustion Institute 40 (2024) 105353.
[26] J. Choe, W. Sun, Experimental investigation of non-equilibrium plasma-assisted ammonia flames using NH_2* chemiluminescence and OH planar laser-induced fluorescence, Proceedings of the Combustion Institute 39 (2023) 5439-5446.
[27] T. Taneja, P. Johnson, S. Yang, Nanosecond pulsed plasma assisted combustion of ammonia-air mixtures: Effects on ignition delays and NO_x emission, Combust. Flame 245 (2022) 112327.
[28] X. Mao, H. Zhong, T. Zhang, A. Starikovskiy, Y. Ju, Modeling of the effects of non-equilibrium excitation and electrode geometry on H_2/air ignition in a nanosecond plasma discharge, Combust. Flame 240 (2022) 112046.
[29] J.K. Lefkowitz, T. Ombrello, An exploration of inter-pulse coupling in nanosecond pulsed high frequency discharge ignition, Combust. Flame 180 (2017) 136–147.
[30] J.K. Lefkowitz, T. Ombrello, Reduction of flame development time in nanosecond pulsed high frequency discharge ignition of flowing mixtures, Combust. Flame 193 (2018) 471–480.
[31] J. Lefkowitz, S. Hammack, C. Carter, T. Ombrello, Elevated OH production from NPHFD and its effect on ignition, Proceedings of the Combustion Institute 38 (2021) 6671-6678.

[32] K. Opacich, T. Ombrello, J. Heyne, J. Lefkowitz, R. Leiweke, K. Busby, Analyzing the ignition differences between conventional spark discharges and nanosecond-pulsed high-frequency discharges, Proceedings of the Combustion Institute 38 (2021) 6615-6622.
[33] M. Castela, B. Fiorina, A. Coussement, O. Gicquel, N. Darabiha, C. O. Laux, Modelling the impact of non-equilibrium discharges on reactive mixtures for simulations of plasma-assisted ignition in turbulent flows, Combust. Flame 166 (2016): 133-147.
[34] Y. Bechane, B. Fiorina, A numerical investigation of plasma-assisted ignition by a burst of nanosecond repetitively pulsed discharges, Combust. Flame 259 (2024): 113106.
[35] T. Taneja, T. Ombrello, J. Lefkowitz, S. Yang, Large eddy simulation of plasma assisted ignition: Effects of pulse repetition frequency, number of pulses, and pulse energy, Combust. Flame 267 (2024): 113574.
[36] N. Barléon, L. Cheng, B. Cuenot, O. Vermorel, A phenomenological model for plasma-assisted combustion with NRP discharges in methane-air mixtures: PACMIND, Combust. Flame 253 (2023): 112794.
[37] X. Mao, H. Zhong, Z. Wang, T. Ombrello, Y. Ju, Effects of inter-pulse coupling on nanosecond pulsed high frequency discharge ignition in a flowing mixture, Proceedings of the Combustion Institute 39 (2023) 5457-5464.
[38] Z. Chen, M. Burke, Y. Ju, Effects of Lewis number and ignition energy on the determination of laminar flame speed using propagating spherical flames, Proceedings of the Combustion Institute 32 (2009) 1253-1260.
[39] Z. Chen, Effects of radiation and compression on propagating spherical flames of methane/air mixtures near the lean flammability limit, Combust. Flame 157 (2010) 2267-2276.
[40] Z. Chen, M. Burke, Y. Ju, On the critical flame radius and minimum ignition energy for spherical flame initiation, Proceedings of the Combustion Institute 33 (2011) 1219-1226.
[41] Z. Chen, Studies on the Initiation, Propagation, and Extinction of Premixed Flames, The Department of Mechanical and Aerospace Engineering, Princeton University, Princeton, NJ, 2009.
[42] W. Sun, Developments of Efficient Numerical Methods for Combustion Modeling with Detailed Chemical Kinetics, The Department of Mechanical and Aerospace Engineering, Princeton University, Princeton, NJ, 2020.
[43] T. Zhang, W. Sun, L. Wang, Y. Ju, Effects of low-temperature chemistry and turbulent transport on knocking formation for stratified dimethyl ether/air mixtures, Combust. Flame 200 (2019) 342–353.
[44] Z. Chen, On the accuracy of laminar flame speeds measured from outwardly propagating spherical flames: Methane/air at normal temperature and pressure, Combust. Flame 162 (2015) 2442-2453.
[45] Y. Wang, W. Han, Z. Chen, Effects of fuel stratification on ignition kernel development and minimum ignition energy of n-decane/air mixtures, Proceedings of the Combustion Institute 37 (2019) 1623-1630.
[46] W. Zhang, M. Faqih, X. Gou, Z. Chen, Numerical study on the transient evolution of a premixed cool flame, Combust. Flame 187 (2018) 129-136.
[47] M. Faghih, H. Li, X. Gou, Z. Chen, On laminar premixed flame propagating into autoigniting mixtures under engine-relevant conditions, Proceedings of the combustion institute 37 (2019) 4673-4680.
[48] L.S. Thorsen, M.S. Jensen, M.S. Pullich, J.M. Christensen, H. Hashemi, P. Glarborg, V.A. Alekseev, E.J. Nilsson, Z. Wang, B. Mei, High pressure oxidation of NH_3/n-heptane mixtures, Combust. Flame 254 (2023) 112785.
[49] H. Zhao, X. Yang, Y. Ju, Kinetic studies of ozone assisted low temperature oxidation of dimethyl ether in a flow reactor using molecular-beam mass spectrometry, Combust. Flame 173 (2016) 187-194.
[50] T.Y. Chen, X. Mao, H. Zhong, Y. Lin, N. Liu, B.M. Goldberg, Y. Ju, and E. Kolemen. Impact of CH_4 addition on the electron properties and electric field dynamics in a Ar nanosecond-pulsed dielectric barrier discharge. Plasma Sources Sci. Technol. 31.12 (2023) 125013.
[51] M. Vorenkamp, S. Steinmetz, X. Mao, Z. Shi, A. Starikovskiy, Y. Ju, and C. Kliewer. Effect of plasma-enhanced low-temperature chemistry on deflagration-to-detonation transition in a microchannel. AIAA J. 61.11 (2023) 4821-4827.
[52] Y. Zhu, X. Chen, Y. Wu, S. Starikovskaia. PASSKEy code [software]. Available from http://www.plasma-

tech.net/parser/passkey/(Science and Technology of Plasma Dynamics Laboratory, Xi'an, China and Laboratoire de Physique des Plasmas, Paris, France, 2021).
[53] Y. Zhu, S. Shcherbanev, B. Baron, S. Starikovskaia, Nanosecond surface dielectric barrier discharge in atmospheric pressure air: I. Measurements and 2D modeling of morphology, propagation and hydrodynamic perturbations, Plasma Sources Sci. Technol. 26 (2017) 125004.
[54] Y. Zhu, X. Chen, Y. Wu, J. Hao, X. Ma, P. Lu, P. Tardiveau, Simulation of the ionization wave discharges: a direct comparison between the fluid model and E–FISH measurements, Plasma Sources Sci. Technol. 30 (2021) 075025.
[55] S. Pancheshnyi, Role of electronegative gas admixtures in streamer start, propagation and branching phenomena, Plasma Sources Science and Technology 14.4 (2005): 645.
[56] X. Mao, Q. Chen, A.C. Rousso, T.Y. Chen, Y. Ju, Effects of controlled nonequilibrium excitation on H2/O2/He ignition using a hybrid repetitive nanosecond and DC discharge, Combust. Flame 206 (2019) 522–535.
[57] G. Hagelaar, L.C. Pitchford, Solving the Boltzmann equation to obtain electron transport coefficients and rate coefficients for fluid models, Plasma sources science and technology 14 (2005) 722.
[58] Law, Chung K. Combustion physics. Cambridge university press, 2010.